Polymer Chemistry

ROYAL SOCIETY OF CHEMISTRY

PAPER

View Article Online
View Journal | View Issue

Cite this: *Polym. Chem.*, 2020, **11**, 7487

Self-assembly of rod-coil block copolymers on a substrate into micrometer-scale ordered stripe nanopatterns†

Zhengmin Tang,[a] Da Li,[a] Jiaping Lin, *[a] Liangshun Zhang, [a] Chunhua Cai, *[a] Yuan Yao, [a] Chunming Yang [b] and Xiaohui Tian[a]

The ability to control the ordering of self-assembled nanostructures is important for block copolymer (BCP) nanotechnology but remains a challenge. Herein, we proposed a facile and feasible approach to generate ordered surface nanostructures *via* the self-assembly of rod-coil BCPs on a substrate. Micrometer-scale, well-aligned, and vertically orientated stripe nanopatterns are readily constructed on the substrate in a fast and controllable way. The feature sizes of the nanopatterns can be adjusted by the molecular weight of BCPs. In addition, self-assembling conditions such as BCP concentration and temperature were found to possess a significant influence on the surface morphology, as well as the order degree of the nanopatterns. Dissipative particle dynamics theoretical simulations provided complementary information for the experimental observations, including the inner chain packing and the dynamic process of the formation of ordered structures. This work presents a novel and effective strategy for the fabrication of well-aligned nanopatterns as an alternative to traditional methods.

Received 3rd October 2020,
Accepted 4th November 2020

DOI: 10.1039/d0py01404d

rsc.li/polymers

Introduction

Self-assembly of block copolymers (BCPs) has attracted considerable attention in nanoscience due to its ability to generate various types of periodic nanostructures. Thin films of BCPs have broad potential applications in nanotechnologies ranging from ultra-high-density storage media to nanoporous membranes and nanolithography.[1–5] The ability to control the lateral ordering and orientation of self-assembled nanostructures of BCPs is important for many of these applications. However, for typical coil–coil BCP self-assembly on a substrate, polycrystalline-type structures with many grain boundaries and defects are spontaneously formed due to the entropy and incomplete annealing. Plenty of methods have been developed to promote the ordered structure formation in BCP thin films by adopting various strategies, such as thermal/solvent-vapor annealing,[6,7] temperature gradient,[8] external electric or magnetic field,[9,10] and the use of chemoepitaxy and graphoepitaxy on substrates.[11–15] However, the utilization of these methods still needs to be optimized and improved. For instance, the solvent-vapor annealing method usually needs complicated procedures that last for hours or days. The fabrication of chemical or topographical pre-patterns requires top-down patterning integrated with traditional photolithography. These multistep procedures significantly increase the time and cost requirements for the ordering of BCPs.

The self-assembly of rod-coil BCPs on a substrate could be a promising and facile way to produce ordered surface nanostructures without complex processes. The tendency for the liquid crystalline ordering between the rod blocks can promote the formation of ordered surface nanostructures at a solvent/substrate interface.[16,17] However, it is challenging to achieve long-range ordering in thin films of rod-coil BCPs because the rigid blocks usually possess a strong crystallization tendency and/or high melting temperature which make the annealing process inefficient.[18–22] Some attempts have been made to construct ordered surface nanostructures of rod-coil BCP thin films on the substrate by approaches such as immersion coating.[23–25] In most cases, however, local-ordered surface nanostructures are generated. One reason could be that the BCPs are usually anchored to the substrate, which limits the mobility of polymer chains, and thus the rod-rod alignment is hampered during the self-assembly process. Therefore, whether the adsorption and assembly of rod-coil BCPs on the

[a]*Shanghai Key Laboratory of Advanced Polymeric Materials, Key Laboratory for Ultrafine Materials of Ministry of Education, Frontiers Science Center for Materiobiology and Dynamic Chemistry, School of Materials Science and Engineering, East China University of Science and Technology, Shanghai 200237, China. E-mail: jlin@ecust.edu.cn, caichunhua@ecust.edu.cn*

[b]*Shanghai Synchrotron Radiation Facility, Shanghai Advanced Research Institute, Chinese Academy of Sciences, Shanghai 201204, China*

†Electronic supplementary information (ESI) available: Polymer synthesis; experimental methods; control experiment; complementary characterization results; DPD theoretical simulations. See DOI: 10.1039/d0py01404d

substrate could produce large-area ordered nanopatterns remains to be further explored. In addition, to date no rigorous efforts have been devoted to controlling the domain ordering of adsorbed layers of BCPs on the substrate.

Herein, we report a facile and feasible approach to fabricate micrometer-scale, well-aligned, and vertically orientated stripe nanopatterns by employing the adsorption and assembly of poly(γ-benzyl-L-glutamate)-*block*-poly(ethylene glycol)(PBLG-*b*-PEG) rod-coil BCPs on the substrate. Such an approach achieves a one-step process of the film formation and pattern ordering, which can be completed within several minutes and without the requirement of subsequent annealing treatments, showing advantages over traditional spin-coating or casting methods. The effects of the molecular weight of BCPs and assembling conditions such as BCP concentration and temperature on the self-assembled morphology were examined by a combination of atomic force microscopy (AFM) and grazing-incidence small-angle X-ray scattering (GISAXS) measurements. Moreover, dissipative particle dynamics (DPD) theoretical simulations were performed to obtain information that is difficult to be obtained from the experiments. Finally, a mechanism was suggested to explain the formation of highly ordered nanostructures on the substrate.

Results and discussion

Well-aligned stripe nanopatterns

The general experimental procedure for the adsorption and self-assembly of PBLG-*b*-PEG BCPs on the substrate is illustrated in Fig. 1a. Firstly, 3 mL of polymer solutions (tetrahydrofuran (THF)/*N*,*N*′-dimethylformamide (DMF), 1/1 v/v, polymer concentration = 0.4 g L^{-1}) and a piece of polystyrene (PS)-coated silicon wafer (PS-silicon) were placed together in a beaker. The coated PS nano-layers (thickness: ~16 nm) were heat treated (temperature: ~160 °C) thus irreversibly adsorbed on the silicon substrate, and the PS could not dissolve in solvents.[26,27] To induce the adsorption-ordering process, water (selective for PEG segments) was subsequently added dropwise. Afterward, the amphiphilic PBLG-*b*-PEG BCPs tend to adsorb onto the hydrophobic PS-silicon substrate to reduce its surface energy. Further addition of water induces the packing and ordering of adsorbed BCP layer into well-aligned nanopatterns over large areas.

Fig. 1b presents the typical AFM topographic image of the morphology self-assembled from $PBLG_{12k}$-*b*-PEG_{5k} (the subscript refers to the number-average molecular weight, M_n, for corresponding segment) BCPs on the PS-silicon substrate at 20 °C. Micrometer-scale well-aligned nanopatterns composed of periodic nanostripes (bright region of the AFM image) were observed. The nanostripes appear much straighter than those commonly observed in the coil–coil BCP films on flat substrates since the locally formed liquid crystalline-like structures can have higher bending energy.[28] In addition, it is evident that the stripe nanopatterns formed in this spontaneous self-assembly process have fewer defects. The average

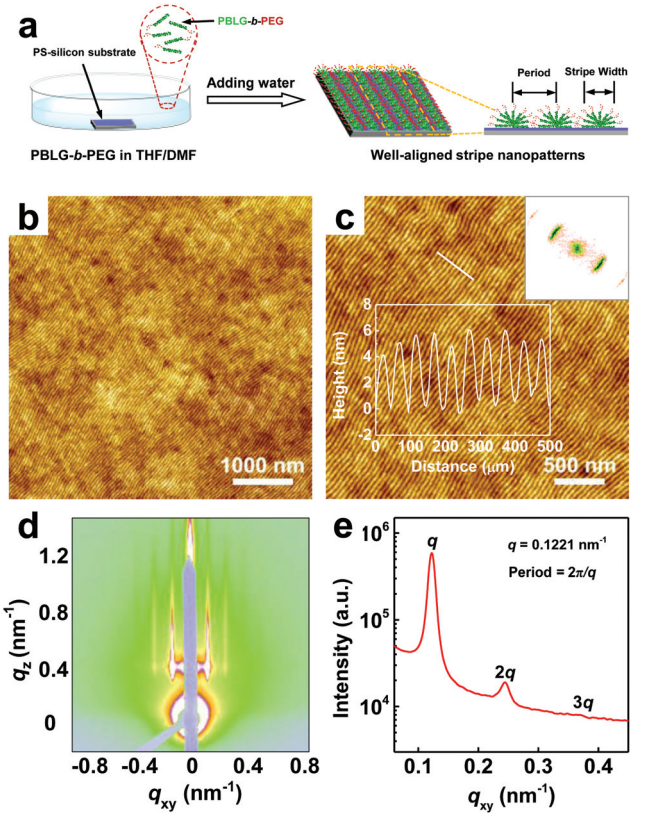

Fig. 1 (a) Schematic illustration of the formation of well-aligned stripe nanopatterns by the adsorption and self-assembly of PBLG-*b*-PEG BCPs on the PS-silicon substrate. (b) AFM topographic image of the well-aligned stripe nanopatterns self-assembled from $PBLG_{12k}$-*b*-PEG_{5k} on the PS-silicon substrate at 20 °C. (c) Close-up AFM image of the well-aligned stripe nanopatterns. The Insets show the fast Fourier transform (FFT) (upper right) of the image and the height profile (bottom left) of the nanopatterns across the white line, respectively. (d) 2D GISAXS pattern of the thin film. (e) 1D GISAXS spectra of the thin film obtained at the q_z value of 0.4 nm^{-1}.

ordered domain size of the stripe nanopatterns is *ca.* 9 μm^2, and a larger ordered domain size up to 25 μm^2 can even be observed (Fig. 1b and Fig. S3†). Fig. 1c shows the close-up AFM image of the well-aligned nanopatterns. The corresponding fast Fourier transform (FFT) and the height profile of the AFM image (see the insets of Fig. 1c) corroborate that the stripe nanopatterns are of good regularity with a period (spacing size) of ~50 nm. The stripe width was measured to be ~22 nm, slightly larger than twice the length of fully extended PBLG rod blocks (8.3 nm), suggesting that the nanostripes may consist of PBLG rods that take a "head-to-head" arrangement perpendicular to the stripe long axis.[29,30] The internal structural information of the thin film was further confirmed by GISAXS technique, through examining a sample area much larger than the one scanned by typical AFM measurements. As seen in Fig. 1d and e, scattering spots with sharp peaks of first- and second-order at q_{xy} = 0.1221 nm^{-1} and q_{xy} = 0.2433 nm^{-1} were observed along the *xy*-direction, indicating that the nanostripes exhibit a perpendicular periodic arrange-

ment (period = 51.4 nm) along the in-plane of the film over a large area. The GISAXS result is consistent with the AFM observations. The thickness of the stripe nanopatterns was determined to be *ca.* 6 nm, which was confirmed by measuring the height of steps obtained by scratching parts of the organic layers off with a razor blade, implying that the BCP film is a monolayer (for details, see Fig. S4 in the ESI†).

The feature sizes of the nanopatterns can be regulated by M_n of a series of BCPs. As can be seen from Fig. 2a–c, $PBLG_{5k}$-*b*-PEG_{2k}, $PBLG_{8k}$-*b*-PEG_{2k}, and $PBLG_{20k}$-*b*-PEG_{5k} BCPs show similar self-assembly behaviors, forming well-aligned stripe nanopatterns with different feature sizes. The stripe width measured from AFM images was plotted in Fig. 2d along with the M_n of PBLG rod blocks. Overall, there is an approximately linear positive correlation between the stripe width and the M_n of PBLG, that is, the stripe width increases from ~12 nm ($PBLG_{5k}$-*b*-PEG_{2k}) to ~16 nm ($PBLG_{8k}$-*b*-PEG_{2k}) and then to ~32 nm ($PBLG_{20k}$-*b*-PEG_{5k}). Meanwhile, the period of the nanopatterns also increases with the M_n of the BCPs from ~29.1 nm ($PBLG_{5k}$-*b*-PEG_{2k}) to ~61.9 nm ($PBLG_{20k}$-*b*-PEG_{5k}) (data is presented in Table 1). These results indicate that the stripe width can be regulated by varying the length of PBLG rod blocks, and the well-aligned stripe nanopatterns are maintained at the higher PBLG content (~80.0 wt% PBLG) and longer copolymer chains. Note that in previous thin-film studies of asymmetric rod-coil BCPs, a relatively long rod block is always found to form disordered fiber-like structures, which limits their practical applications.[20,31] The method employed in the present system, on the other hand, is advantageous for the formation of well-aligned patterns even though the content of PBLG rod blocks is high (up to ~85.7 wt% PBLG). However, it is noted that discrete nanofibers are obtained on the PS-silicon substrate when the molecular weight of PBLG blocks becomes much larger (*e.g.*, M_n = 66 kg mol^{-1}, ~92.9 wt% PBLG) (Fig. S5, ESI†).

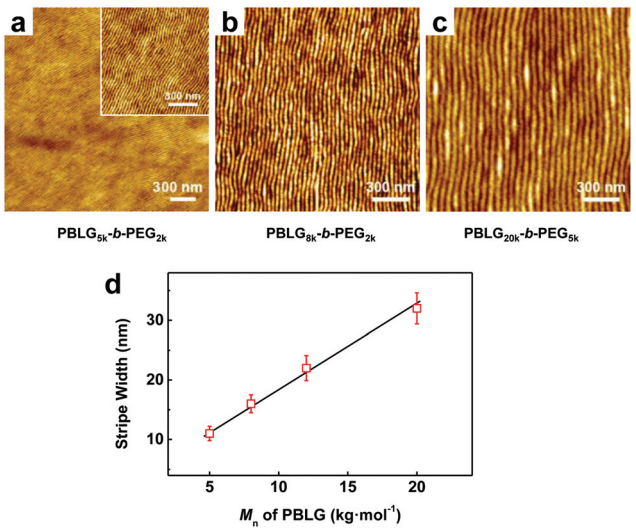

Fig. 2 (a–c) AFM images of the well-aligned stripe nanopatterns self-assembled form a series of asymmetric BCPs with different M_n on the PS-silicon substrate: (a) $PBLG_{5k}$-*b*-PEG_{2k} (71.4 wt% PBLG), inset shows the close-up AFM image of the nanopatterns, (b) $PBLG_{8k}$-*b*-PEG_{2k} (80.0 wt% PBLG), and (c) $PBLG_{20k}$-*b*-PEG_{5k} (80.0 wt% PBLG). (d) Dependence of the stripe width on the M_n of the PBLG blocks.

Table 1 Characteristics of the nanopatterns

Sample	L_{PBLG}[a] (nm)	Stripe width[b] (nm)	Period[c] (nm)
$PBLG_{5k}$-*b*-PEG_{2k}	3.4	~12	~29.1
$PBLG_{8k}$-*b*-PEG_{2k}	5.5	~16	~35.8
$PBLG_{12k}$-*b*-PEG_{5k}	8.3	~22	~51.4
$PBLG_{20k}$-*b*-PEG_{5k}	13.8	~32	~61.9

[a] The length of PBLG blocks was calculated based on the α-helix conformation model. [b] The stripe width of the PBLG domain was measured by AFM. [c] The period of the nanopatterns was obtained from AFM measurements.

Chain packing model revealed by dissipative particle dynamics (DPD) simulations

It has been widely documented that self-assembly of amphiphilic BCPs at an interface between the hydrophobic substrate and aqueous solutions can generate surface micelles.[17,32] Considering the geometrical relationship between the stripe width (~22 nm) and the thickness (~6 nm) of the well-aligned nanopatterns formed by $PBLG_{12k}$-*b*-PEG_{5k}, it is reasonable to speculate that the nanopatterns could be composed of surface micelles. To complement the experiments, we carried out DPD simulations to explore the inherent structures of the nanopatterns. In DPD simulations, a coarse-grained model containing a planar substrate and R_4C_4 (R for rigid PBLG, and C for flexible PEG) rod-coil BCPs was constructed to represent the system consisting of the PS-silicon substrate and $PBLG_{12k}$-*b*-PEG_{5k} BCPs (Fig. 3a). The interaction parameters between each component were set corresponding to the experimental examples, that is, a_{RC} = 80, a_{RS} = 80, a_{RP} = 25, a_{CP} = 30, a_{CS} = 30, and a_{PS} = 120, where R, C, S, and P stand for rods, coils, solvents, and the planar substrate (see Table 2). As shown in Fig. 3b, the stripe nanopatterns are well reproduced by the DPD simulation. The cross-sectional images of the patterns reveal that the stripes are "semi-cylinder" surface aggregates adhered to the substrate, where the hydrophobic rod blocks from the inner parts of the stripes that are wrapped by the hydrophilic coils outside (Fig. 3c). The rods are packed in a "head-to-head" fashion. To describe the chain distributions, we further measured the orientation angle α (for the definition, see the inset of Fig. 3d) between the rods and planar substrate. Fig. 3d presents the probability distribution of the α value. It was found that ~34% of the angles are distributed in the range of 0–10° while only 1.45% of the angles are distributed in the range of 80–90°. This result suggests that the rods tend to lie down on the substrate as the hydrophobic rod blocks have a strong affinity to the hydrophobic substrate. Moreover, the rod blocks adjacent to the substrate tend to be perpendicular to the stripe long axis (Fig. 3c and Fig. S6d†). Accordingly, it can be deduced that the PBLG rods are packed

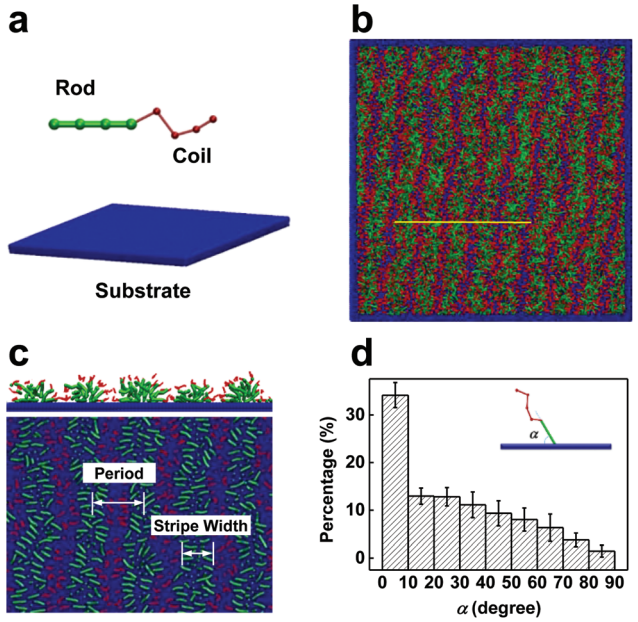

Fig. 3 (a) The DPD model containing rod-coil BCPs (denoted by R_4C_4) and a planar substrate (P). (b) Stripe nanopatterns well calculated by DPD simulations. (c) Cross-sectional images of the stripe nanopatterns along the yellow line in Fig. 3b. Solvents are not shown in Fig. 3a–c. (d) The probability distribution of the angle α, where the inset shows the definition of the angle α.

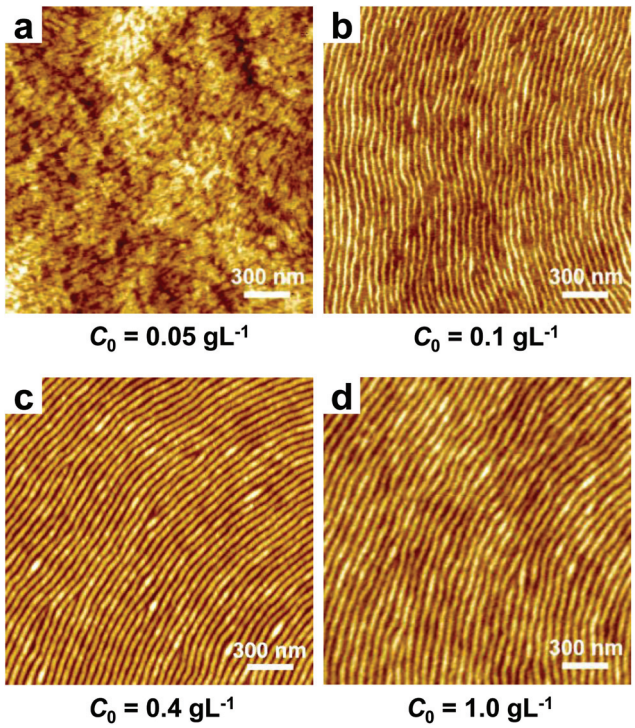

Fig. 4 AFM images of the morphology self-assembled from $PBLG_{12k}$-*b*-PEG_{5k} BCPs on the PS-silicon substrate with various initial block copolymer concentrations (C_0): (a) C_0 = 0.05 g L^{-1}, (b) C_0 = 0.1 g L^{-1}, (c) C_0 = 0.4 g L^{-1}, and (d) C_0 = 1.0 g L^{-1}.

Table 2 Interaction parameter a_{ij} set in the DPD simulations

a_{ij}	R (rod)	C (coil)	S (solvent)	P (PS)
R (rod)	25			
C (coil)	80	25		
S (solvent)	30–80	30	25	
P (PS)	25	30	120	25

perpendicular to the stripe axis, resembling the liquid crystalline structure. Taking this packing model into consideration, we can take twice the BCP length as the period approximately (Fig. 3c). The simulation results can well support the experimental observations and verify the speculation that the stripe nanopatterns are the semi-micelles.

Effects of BCP concentration and temperature on surface morphology

To develop knowledge of the adsorption-assembly of PBLG-*b*-PEG BCPs on the substrate, we examined the effects of self-assembling conditions on the self-assembled morphology. The influence of initial BCP concentration (C_0) was first examined. As shown in Fig. 4a, when C_0 = 0.05 g L^{-1}, no characteristic morphology was observed on the PS-silicon substrate. When increasing the C_0 to 0.1 g L^{-1}, it was found that disconnected and winding stripes are formed on the substrate (Fig. 4b). Further upon increasing the C_0 to 0.4 and then to 1.0 g L^{-1}, robust and well-aligned stripe nanopatterns were observed (Fig. 4c and d). In the systems, the copolymers can be either adsorbed onto the PS-silicon substrate or form micelles in solutions to reduce the total free energy. When the C_0 value is lower, the copolymers tend to adsorb onto the surface of PS-silicon to minimize the interfacial energy as long as the surface has not yet reached saturation. In this situation, the stripe morphology is immature and becomes evident with increasing BCP concentrations (Fig. 4a–c). When the C_0 value is higher, the adsorption of copolymers on the PS-silicon substrate is saturated, and the excess copolymers are dispersed in solutions to form small aggregates (Fig. S7, ESI†). The stripe morphology does not change significantly on the substrate at high C_0 (Fig. 4c and d). This is probably because the stripes are wrapped by the hydrophilic PEG chains (Fig. 3c), which prevents the fusion of micelles from solutions with the adsorbed BCP layer.

In addition to the BCP concentration, the assembling temperature was found to be another important factor influencing the self-assembled morphology. Fig. 5 shows the resulting morphology for each sample obtained in the temperature ranging from 20 to 40 °C (the C_0 is fixed at 0.4 g L^{-1}). As can be seen from Fig. 5a–e, appreciable changes have been observed on the stripe nanopatterns with increasing temperatures, and the stripes disconnect and swell randomly at higher temperatures. Nevertheless, the stripes produced at all the experimental temperatures exhibit a periodic arrangement. To in-depth understand the pattern ordering, we carried out GISAXS measurements on these samples prepared at 20 to

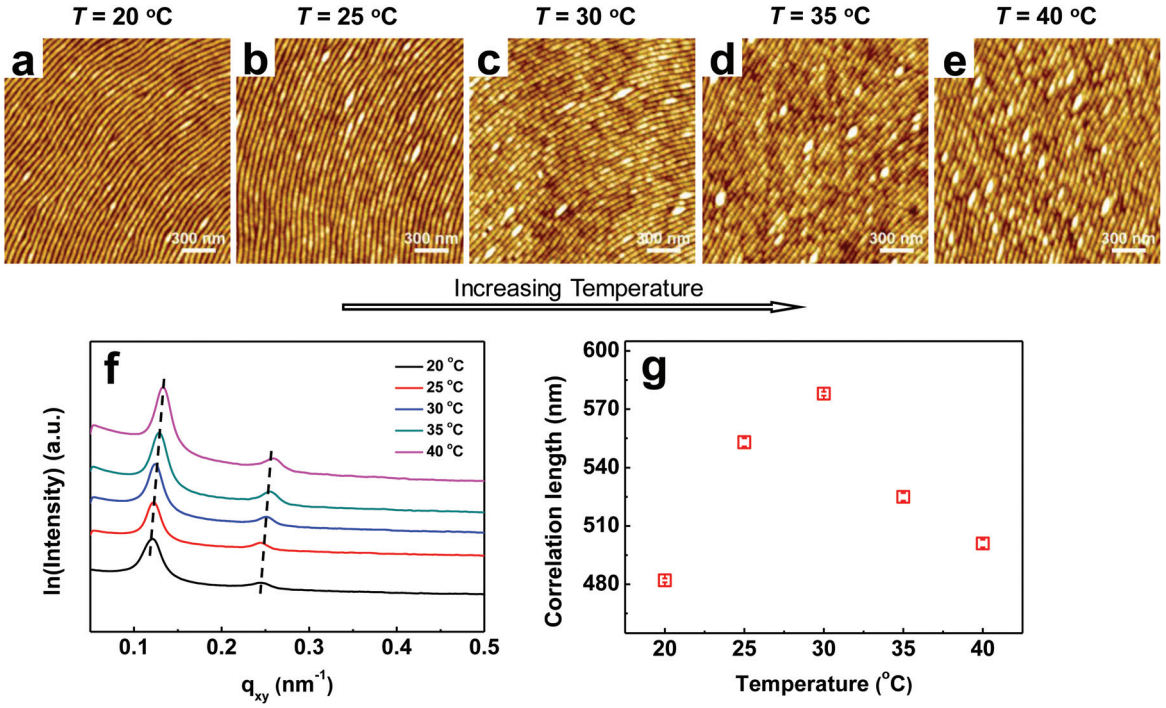

Fig. 5 (a–e) AFM images of the morphologies self-assembled from $PBLG_{12k}$-*b*-PEG_{5k} BCPs on the PS-silicon substrate at various temperatures: (a) 20 °C, (b) 25 °C, (c) 30 °C, (d) 35 °C, and (e) 40 °C. (f) The relative intensity profiles along q_{xy} obtained from the GISAXS patterns corresponding to the temperatures. The dashed lines mark the shifted first and second scattering peaks, which indicate the shift of the period with increasing temperatures. (g) The correlation length calculated from the full width at half-maximum (fwhm) of the main peak shown in Fig. 5f.

40 °C. Fig. 5f shows the relative intensity profiles along the *xy*-plane obtained from the 2D GISAXS patterns (Fig. S8†). For the samples prepared at 20 to 40 °C, the period varies slightly from 51.5 nm to 46.3 nm (corresponding to the shift of sharp peaks), which could be mainly attributed to the shrink of PEG segments at higher temperatures.[33] Moreover, we can quantitatively determine the in-plane order degree of the stripe nanopatterns through calculating the correlation length parameter, ξ, which is inversely proportional to the half-maximum width (Δq_{xy}) of the peak. The stripe nanopatterns can be regarded as composed of randomly oriented grains, where each grain consists of a set of perfectly ordered straight stripes.[34] The correlation length parameter, ξ, is defined as the average diameter of the grain, calculated through the classical Scherrer formula:[35]

$$\xi = K\frac{2\pi}{\Delta q_{xy}} \quad (1)$$

where K (= 1.03) is a constant related to the grain shape. The calculated values of ξ are presented in Fig. 5g. As the assembling temperature increases from 20 to 30 °C, the value of ξ increases, indicating the enhanced ordering of stripe nanopatterns. Further increasing the assembling temperature, the value of ξ falls, corresponding to the decrease of ordering degree. The variation of ξ values can be rationalized by considering the stripe morphology. As shown in Fig. 5a–e, the stripes become straighter as the assembling temperature increases. This can lead to an increase in the ordering of nanopatterns due to the more orderly arrangement of stripes in one direction. However, when the assembling temperature is above 30 °C, the disconnected stripes would destroy the periodicity of the stripe nanopatterns. As a result, the ordering degree of stripe nanopatterns decreases. We also found that the initial THF/DMF ratios can affect the self-assembled surface morphology. When the content of DMF is lower, the formed stripe nanopatterns are well-ordered at all the experimental temperatures, while disordered structures appear when the content of DMF is higher (Fig. S9 and 10, ESI†).

The substrate also has a pronounced influence on the morphology of adsorbed BCP layers. The assemblies of $PBLG_{12k}$-*b*-PEG_{5k} BCPs on various substrates were investigated. We firstly prepared a substrate with a clear step-edge between the PS surface and the bared Si substrate (Fig. S11a†). As compared with the Si surface, the PS surface is much more attractive to the BCPs. As a result, the well-aligned nanopatterns are selectively formed in the PS region, while some disordered aggregates are formed in the Si region (Fig. S11b†). We also examined the influence of various polymer-coated substrates on the self-assembled morphology. Two kinds of substrates were prepared, one was the polymethyl methacrylate (PMMA, less hydrophobic)-coated substrate, and the other was the poly(2-vinylphridine) (P2VP, hydrophilic)-coated substrate. It was found that island-like structures are formed on the PMMA sub-

strate, and no aggregates are formed on the hydrophilic P2VP substrate (Fig. S11c and d†). These results suggest that the strong interactions between the substrate and the BCPs are necessary conditions for the formation of well-aligned stripe nanopatterns.

Dynamic process of the formation of well-aligned nanopatterns

To understand how the PBLG-*b*-PEG BCPs assemble into ordered nanopatterns on the substrate, we examined the morphological evolution of the nanopatterns by monitoring the self-assembly progress at various solvent conditions. We firstly measured the critical water content (CWC) at which the PBLG-*b*-PEG BCPs begin to aggregate in solutions, by recording abrupt turbidity changes during the process of adding water.[36] As revealed by the turbidity curve, the CWC for $PBLG_{12k}$-*b*-PEG_{5k} is 14.4 vol% (Fig. 6a). Since the PS nano-layer is irreversibly absorbed on Si substrate, we can rule out the possibility that the PS segments dissolve in solutions to participate in the self-assembly process. Fig. 6b–e shows the AFM images of the dried thin films of self-assembled morphology taken at various water contents. The sample prepared in a solution of 11.7 vol% of water shows fuzzy features on the substrate due to a lower water content below the CWC (Fig. 6b). When the added water content reaches 18.3 vol%, scattered and short stripes appear, suggesting that the PBLG-*b*-PEG BCPs have been absorbed onto the surface of the PS-silicon substrate (Fig. 6c). Compact and long stripes appear when the water content reaches 25.0 vol%, indicating that the BCPs start to pack into local-ordered nanostructures on the PS-silicon substrate (Fig. 6d). Further increasing water content to 31.7 vol%, the stripes rearrange to form ordered stripe nanopatterns (Fig. 6e). The stripe width obtained at the water content of 31.7 vol% is much narrower than that obtained at the water content of 25.0 vol% (~22 nm and ~31 nm). These observations indicate that the formation of well-aligned nanopatterns includes the adsorption of copolymers on the substrate and the subsequent structural reconstruction, which is driven by the minimum of the energetically unfavorable surface area.[37] Importantly, the rod-rod alignment between the PBLG blocks is essential to the formation of well-aligned nanostructures. In a control experiment, PS-*b*-PEG coil–coil BCPs were used to assemble on the surface of the PS-silicon substrate under the same experimental conditions. It was found that irregular structures instead of ordered stripe nanopatterns are obtained on the substrate (Fig. S12, ESI†).

The pattern evolution on the substrate was also studied by DPD to obtain complemental information. In the simulations, we varied the solvent selectivity parameter (a_{RS}) from 30 to 80 in a step-by-step manner, corresponding to the water addition process in the experiments. Fig. 7a presents the equilibrium structures obtained at various a_{RS}. As can be seen, when the solvent selectivity is weaker at the beginning of the self-assembly, the BCPs are dispersed randomly in the simulation box (a_{RS} = 30). With increasing the solvent selectivity, the BCPs are

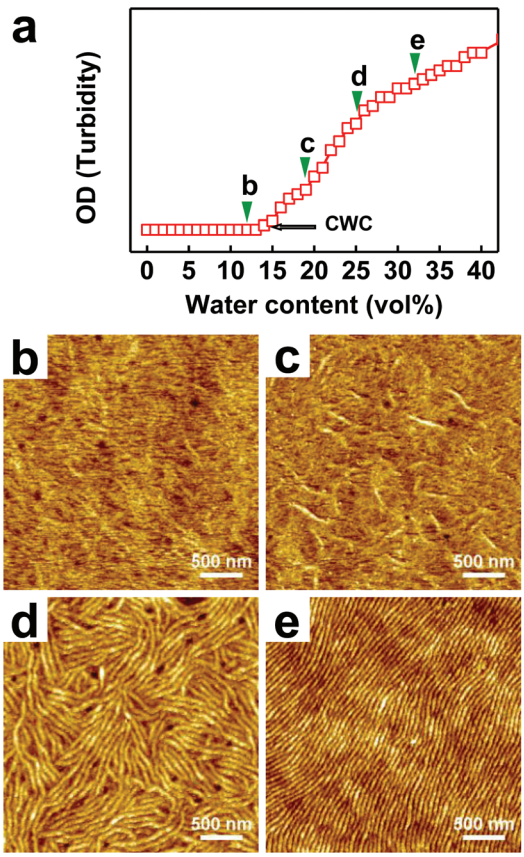

Fig. 6 (a) Turbidity (optical density) curve of $PBLG_{12k}$-*b*-PEG_{5k} block copolymers as a function of added water content to the solution. (b–e) AFM images of the morphological evolution of the stripe patterns at various water contents: (b) 11.7 vol%, (c) 18.3 vol%, (d) 25.0 vol% and (e) 31.7 vol%.

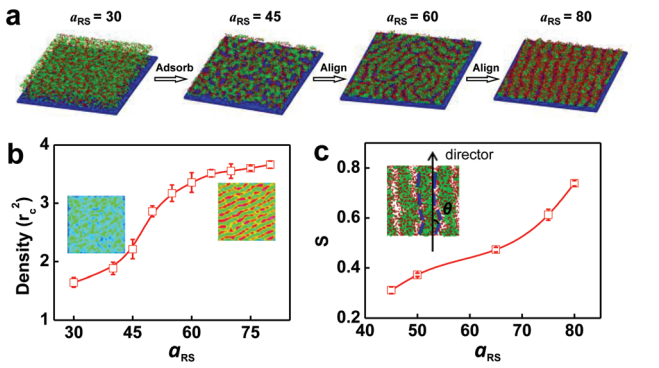

Fig. 7 (a) Morphological evolution of the stripe patterns on the planar substrate at various solvent conditions revealed by DPD simulations. The a_{RS} parameter represents the solvent selectivity (water content). (b) Profile of the measured density of rod blocks adsorbed on the substrate at various solvent conditions. Inserts show the density distribution patterns obtained from a_{RS} = 30 (left side) and a_{RS} = 80 (right side), respectively. (c) Profile of the order parameter (*S*) of the stripe patterns obtained from the simulation results at various solvent conditions. Inset shows the illustration for the angle θ between the local tangent vector of the interface (blue dashed line) and the director.

adsorbed onto the substrate and self-assemble into small aggregates (a_{RS} = 45), which subsequently fuse to form stripe structures as the solvent selectivity becomes larger (a_{RS} = 60). However, the patterns contain a few defects in this state. With further increasing the a_{RS} to 80, the defects are eliminated and the well-aligned stripe nanopatterns were observed. The simulation results well reproduce the water-content-dependent morphological evolution of the nanopatterns observed in the experiments.

Additionally, the simulation results can provide more intuitive information about the adsorption-assembly process of copolymer chains on the substrate. The density changes of the rod blocks adsorbed on the substrate were measured at various solvent conditions. Fig. 7b shows that the density of the rod blocks on the substrate increases progressively with increasing the solvent selectivity (a_{RS}). When a_{RS} is larger than 60, the density of the rod blocks on the substrate increases slowly and reaches the plateau, indicating that most copolymer chains have been adsorbed onto the substrate and a saturation state has been reached. The inserts in Fig. 7b show the 2D density distribution of rod blocks on the substrate obtained at a_{RS} = 30 and a_{RS} = 80, respectively. The blue and red colors are assigned to the lower and higher densities of rod blocks on the substrate, respectively. The inserts clearly show that the rod blocks change from lower density with a disordered state to higher density with ordered patterns on the substrate.

The evolution of the pattern ordering in the self-assembly process is an important issue that needs to be addressed. To quantitatively describe the ordering of the stripe nanopatterns obtained with various a_{RS} in simulations, we introduced an order parameter, S, which is defined as:

$$S = \frac{1}{2}(3\cos^2\theta - 1) \quad (2)$$

where θ is the angle between the local tangent vector of interface (blue dashed line) and the director (see the inset of Fig. 7c). Here, when the S value is close to 1, perfectly ordered patterns are produced on the substrate. Fig. 7c shows the S values of the patterns on the substrate with various a_{RS}. We calculated the S at a_{RS} = 45 because the density of BCPs on the substrate is too low to calculate the accurate order parameters when a_{RS} is smaller. As shown in Fig. 7c, the S increases with increasing a_{RS}, indicating that the ordering of the stripe nanopatterns increases with the addition of water. The max S is 0.73 (a_{RS} = 80) though the pattern in this situation is well-ordered. The reason could be that the stripes are not perfectly straight, and a slight bend of stripes decreases the S value. The simulation results serve as a theoretical support for the understanding of the disorder-to-order transition of the stripe nanopatterns observed in the experiments.

Mechanism of the formation of well-aligned nanopatterns

Based on the results of experiments and simulations, a mechanism is suggested to explain the formation of well-aligned nanopatterns on the PS-silicon substrate. The PBLG-*b*-PEG BCPs are randomly dispersed in initial organic solvents, and the surface of the immersed PS-silicon substrate is stable. The PS segments are more hydrophobic than PBLG segments in aqueous solutions.[17] When water is added, the surface energy of the PS surface increases. To reduce the surface energy, the amphiphilic PBLG-*b*-PEG BCPs, which can be regarded as a kind of macromolecular surfactants, are adsorbed onto the PS-silicon substrate. The attractive interactions between PS surface and PBLG-*b*-PEG BCPs are attributed to hydrophobic interactions and dipolar π–π stacking of phenyl groups. The PS surface adsorbs not only the free copolymer chains, but also the aggregates of copolymers formed in solution as long as the surface has not reached saturation. This is because that the aggregates are unstable in solution, and they tend to be adsorbed onto the PS surface to lower the system energy.[38]

When the water is continuously added and exceeds the CWC, the solubility of PBLG segments also decreases gradually. To reduce the exposure of the PBLG segments to the selective solvent (water), the BCPs self-assemble into stripe-like micelle structures on the substrate, where the PBLG rods pack in an ordered manner in the core, and the PEG coils wrap the core outside. The α-helical PBLG rods and rod-coil architecture of copolymers possess the structural conditions that are necessary for the formation of the stripes: the rigidity of the PBLG rods drives a liquid crystalline-like rod-rod alignment, while the PEG segments stretch out to stabilize the structures (Fig. 3). The anisotropic rod-like stripes subsequently align and rearrange to reduce the free energy of the system, forming ordered stripe nanopatterns on the substrate (Fig. 6). This orderly packing mechanism agrees with the entropy-driven alignment of anisotropic rigid objects.[39]

The above results demonstrate that the adsorption and assembly of rod-coil BCPs on the substrate could be an alternative strategy for constructing well-aligned nanopatterns over large areas. In traditional methods such as spin-coating or casting, the structures can be easily "frozen" in the initial films due to the rapid solvent evaporation. Therefore, thin films usually require additional heat or solvent annealing to access the equilibrium of the microphase separated structures. The solvent annealing process can promote the polymer chain mobility and enhance the pattern ordering.[40] However, the annealing process cannot effectively eliminate the structural defects for the conventional coil–coil BCPs on flat substrates or unguided external fields. In addition, the effect of solvent annealing also depends on the property of the vapors and annealing time, which limits the practical applications. The present method can overcome such drawbacks and achieve a one-step process of the film formation and pattern ordering, which can be completed in a short time (within several minutes) and without the requirement of subsequent annealing treatments. The fluidity of liquid crystalline-like structure contributes to the orderly rod-rod alignment. Moreover, the chemical incompatibility between rod and coil blocks can be adjusted by introducing selective solvents into the assembly systems to accelerate the formation of well-aligned nanopatterns even though the PBLG-*b*-PEG BCPs are highly asymmetric. The present method also makes it possible to create a

large diversity of morphologies by the adsorption-assembly of rod-coil BCPs on various types of PS patterned substrates.

The sustained pursuit of ultrasmall periodic nanostructures is the focus of new-generation nanolithography. We note that the current systems could provide a platform for constructing ultrasmall structures. For typical BCPs, the microphase separation is associated with chemical incompatibility, that is, the product of the Flory–Huggins interaction parameter (χ) and the overall degree of polymerization (N). To enable sub-10 nm nanopatterning, the BCPs with a higher χ are required to produce the microphase separated ordered morphology. A higher χ often results from blocks consisting of highly immiscible components such as inorganic silicon.[41–43] However, due to the limited choices of high-χ BCPs, and considering the difficulties in annealing processing and orientation controlling, the formation of vertically orientated structures with a sharp interface at sub-10 nm length scale remains a challenge. In contrast with the coil–coil BCPs, the entropic loss of rod-coil BCPs is much smaller during the microphase separation. Therefore, a smaller chemical incompatibility of rod-coil BCPs can be enough to drive the microphase separation.[44,45] Recent advances have shown that the formation of sub-5 nm structures can be realized by the self-assembly of liquid crystalline oligomers.[46,47] For the adsorption-assembly procedure, the refinement of the molecular architecture of rod-coil BCPs could be essential to fabricate the structures with sub-5 nm features, which is the focus of future related works.

Micrometer-scale, well-aligned, and vertically orientated stripe nanopatterns have broad interests in polymer nanoscience, and serve as promising materials in emerging nanotechnologies, for example, ultra-high-density storage media, and BCP nanolithography. The research results not only enrich our knowledge about the adsorption-assembly of amphiphilic rod-coil BCPs on the substrate, but also can expand the application of polypeptide-based copolymers in biomedical fields, for instance, biosensors, biomineralization, and protein arrays.[48–50] Specifically, for the PBLG-*b*-PEG BCPs, conventional spin-coating and annealing methods have been shown limited in constructing well-ordered structures (Fig. S13†).

Conclusions

We demonstrate that micrometer-scale well-aligned stripe nanopatterns composed of PBLG-*b*-PEG BCPs can be readily constructed on the substrate in a facile and controllable way. The experiment-simulation combined results reveal that these closely packed stripes are "semi-cylinder" surface micelles and adhered to the substrate. The stripe width and period of the nanopatterns can be adjusted by varying the molecular weight of BCPs. Moreover, the effects of BCP concentration and assembling temperature on the surface morphology were elucidated. It was found that well-aligned stripe nanopatterns can be obtained at high concentrations, and the temperature also influences the stripe morphology as well as the order degree of the nanopatterns. The interplay of the strong attractive interactions between the PS surface and the PBLG-*b*-PEG and an ordered packing tendency of PBLG rod segments is responsible for the formation of well-aligned stripe nanopatterns. The present work can guide the fabrication of ordered surface nanostructures/nanopatterns of BCPs containing rod-type segments with controllable size, orientation and surface morphology, which could have potential applications in nanotemplating, nanolithography, and bioengineering.

Experimental section

Polymer synthesis

PBLG-*b*-PEG BCPs were synthesized *via* ring-opening polymerization of γ-benzyl-L-glutamate-*N*-carboxyanhydride (BLG-NCA) monomers using anhydrous mPEG-NH_2 (M_n = 2 or 5 kg mol^{-1}) as macroinitiators.[51,52] The polymerization was conducted in a reaction bottle placed in the glove box with nitrogen atmosphere. The reaction time was 3 days and the temperature was fixed at 15 °C. After reaction, the products were poured into large amounts of anhydrous ethanol. The precipitates were collected by centrifugation. To purify the polymers, the resulting products were dissolved in chloroform and then precipitated with large amounts of anhydrous ethanol. Details about the polymer synthesis and characterizations are provided in section 1.1 of ESI.†

Preparation of PS-silicon substrate

The monodisperse PS homopolymers were dissolved in toluene with the concentration of ~2.5 wt%. Si (100) wafers (covered with a native oxide layer) were cleaned by immersion in a piranha solution (*i.e.*, H_2SO_4/H_2O_2 = 3/1, v/v) for 30 min and rinsed with a great amount of deionized water and dried with nitrogen gun. The PS-coated substrates (*i.e.*, ultrathin and flattened PS nano-layer irreversibly adsorbed on Si substrate) were prepared according to literatures.[26,53] Firstly, the PS films were prepared by spin-coating the polymer solutions onto cleaned Si substrates. The spin-cast PS films were then heat treated at ~160 °C for 3 days under vacuum. Afterward, the films were soaked in a fresh good solvent of toluene and rinsed for more than ten times. The remaining PS nano-layers were irreversibly adsorbed on Si substrates and insoluble in solvents.[26,27] The obtained PS-silicon wafers were dried in a vacuum oven at 70 °C for 12 h to remove any excess solvent before further experiments. More information about the substrate preparation can be found in section 1.1 of ESI.†

Self-assembly of PBLG-*b*-PEG on the PS-silicon substrate

Firstly, PBLG-*b*-PEG BCPs were dissolved in v/v = 1/1 mixtures of THF and DMF. Then 3 mL of polymer solutions and a piece of PS-silicon wafer were placed together in a beaker. Subsequently, 1.2 mL of deionized water was added dropwise into the polymer solution at a rate of *ca.* 100 μL min^{-1} with slight stirring. Finally, the samples were taken out from the solution and rinsed with a large volume of deionized water.

The samples were dried in a vacuum oven for 12 h at room temperature. More experimental details about the self-assembly process are available in section 1.1 of ESI.†

Characterizations

The morphologies formed on the substrate were characterized by atomic force microscopy (AFM, XE-100, Park Systems) and grazing-incidence small-angle X-ray scattering (GISAXS) measurements. AFM testing was carried out using the non-contact mode, and the scan rate was 0.5 Hz. The obtained images were analyzed using XEI software (Park Systems). GISAXS experiments were performed at the Shanghai Synchrotron Radiation Facility (SSRF, China) 16B beamline. The wavelength of the X-ray was 0.124 nm (E = 10 keV). To probe the surface and inner structure of the nanopatterns, for each sample, the X-ray incident angle was chosen as 0.3° (above the critical angle), and the exposure time was 100 s. Detailed information about the characterizations is provided in section 1.2 of ESI.†

Simulation methods

Dissipative particle dynamics (DPD) simulation was proposed by Koelman and Hoogerbrugge,[54] and developed by Patrick and Robert.[55] Details about the DPD method and the parameter settings can refer to our previous work.[56–58] In this work, a DPD model containing a planar substrate and rod-coil BCPs was constructed to represent the PS substrate and $PBLG_{12k}$-*b*-PEG_{5k}, respectively (see Fig. 3a). The BCPs were mapped into R_4C_4, where four R beads constitute rod block and four C beads constitute coil block (the choice of bead numbers corresponds to the experimental examples). To keep the rigidity of rod blocks, the R beads were restricted by angle forces. The equilibrium bond length of $0.7r_c$ was set for the bonding force, where r_c is the length unit. The C beads adopted flexible polymeric chain conformation. Solvents were modeled as single beads, represented by S. The PS substrate was modeled by two layers of beads (denoted by P) that were closely packed so that the BCPs and solvents cannot permeate through the substrate. The time unit τ was determined by $\tau = (mr_c^2/k_BT)^{1/2}$, where m, and k_BT represent the mass and energy in the simulation, respectively. All simulations were carried out under the NVT ensemble in $60 \times 60 \times 10r_c^3$ boxes with periodic boundary conditions. The interaction parameter a_{ij} (the repulsive parameter between two arbitrary beads i and j) between each type of DPD beads is given in Table 2. All interaction parameters were set corresponding to the experiments. A modified velocity-Verlet algorithm was used to integrate the motion equation, with the time step $\Delta t = 0.01\ \tau$. Over 3×10^6 simulation steps were offered to ensure the equilibrium states have been reached. More simulation details are available in section 1.3 of ESI.†

Conflicts of interest

There are no conflicts to declare.

Acknowledgements

This work was supported by the National Natural Science Foundation of China (51833003, 51621002, and 21975073). Support from Project of Shanghai Municipality (20ZR1471300) is also appreciated.

Notes and references

1 R. A. Segalman, *Mater. Sci. Eng., R*, 2005, **48**, 191–226.
2 I. W. Hamley, *Prog. Polym. Sci.*, 2009, **34**, 1161–1210.
3 W. Wang, C. Du, X. Wang, X. He, J. Lin, L. Li and S. Lin, *Angew. Chem., Int. Ed.*, 2014, **53**, 12116–12119.
4 R. Ruiz, H. Kang, F. A. Detcheverry, E. Dobisz, D. S. Kercher, T. R. Albrecht, J. J. de Pablo and P. F. Nealey, *Science*, 2008, **321**, 936–939.
5 J. Chai and J. M. Buriak, *ACS Nano*, 2008, **2**, 489–501.
6 K. W. Gotrik, A. F. Hannon, J. G. Son, B. Keller, A. Alexander-Katz and C. A. Ross, *ACS Nano*, 2012, **6**, 8052–8059.
7 Y. S. Jung and C. A. Ross, *Adv. Mater.*, 2009, **21**, 2540–2545.
8 B. C. Berry, A. W. Bosse, J. F. Douglas, R. L. Jones and A. Karim, *Nano Lett.*, 2007, **7**, 2789–2794.
9 Y. Rokhlenko, M. Gopinadhan, C. O. Osuji, K. Zhang, C. S. O'Hern, S. R. Larson, P. Gopalan, P. W. Majewski and K. G. Yager, *Phys. Rev. Lett.*, 2015, **115**, 258302.
10 V. Olszowka, M. Hund, V. Kuntermann, S. Scherdel, L. Tsarkova and A. Böker, *ACS Nano*, 2009, **3**, 1091–1096.
11 L. Zhang, L. Wang and J. Lin, *ACS Macro Lett.*, 2014, **3**, 712–716.
12 J. Choi, J. Huh, K. R. Carter and T. P. Russell, *ACS Nano*, 2016, **10**, 7915–7925.
13 W. H. Li and M. Muller, *Prog. Polym. Sci.*, 2016, **54–55**, 47–75.
14 G. Yang, G. Wu, X. Chen, S. Xiong, C. G. Arges, S. Ji, P. F. Nealey, X. Lu, D. J. Darensbourg and Z. Xu, *Nano Lett.*, 2017, **17**, 1233–1239.
15 S. Ji, L. Wan, C. C. Liu and P. F. Nealey, *Prog. Polym. Sci.*, 2016, **54–55**, 76–127.
16 C. Cai, Y. Li, J. Lin, L. Wang, S. Lin, X. S. Wang and T. Jiang, *Angew. Chem., Int. Ed.*, 2013, **52**, 7732–7736.
17 W. Xu, Z. Xu, C. Cai, J. Lin, S. Zhang, L. Zhang, S. Lin, Y. Yao and H. Qi, *J. Phys. Chem. Lett.*, 2019, **10**, 6375–6381.
18 C. H. Braun, B. Schopf, C. Ngov, C. Brochon, G. Hadziioannou, E. J. Crossland and S. Ludwigs, *Macromol. Rapid Commun.*, 2011, **32**, 813–819.
19 H. C. Moon, D. Bae and J. K. Kim, *Macromolecules*, 2012, **45**, 5201–5207.
20 E. Ibarboure and J. Rodriguez-Hernandez, *Eur. Polym. J.*, 2010, **46**, 891–899.
21 M. H. M. Cativo, D. K. Kim, R. A. Riggleman, K. G. Yager, S. S. Nonnenmann, H. Chao, D. A. Bonnell, C. T. Black, C. R. Kagan and S.-J. Park, *ACS Nano*, 2014, **8**, 12755–12762.
22 Y. Yin, D. Zhai, S. Chen, X. Shang, L. Li and J. Peng, *Acta Polym. Sin.*, 2020, **51**, 434–447.

23 J. W. Park and Y. H. Cho, *Langmuir*, 2006, **22**, 10898–10903.
24 J. W. Park, H. Kim and M. Han, *Chem. Soc. Rev.*, 2010, **39**, 2935–2947.
25 L. Wang, Z. Tang, D. Li, J. Lin and Z. Guan, *Nanoscale*, 2020, **12**, 13119–13128.
26 Y. Fujii, Z. Yang, J. Leach, H. Atarashi, K. Tanaka and O. K. C. Tsui, *Macromolecules*, 2009, **42**, 7418–7422.
27 C. Housmans, M. Sferrazza and S. Napolitano, *Macromolecules*, 2014, **47**, 3390–3393.
28 B. D. Olsen, X. F. Li, J. Wang and R. A. Segalman, *Macromolecules*, 2007, **40**, 3287–3295.
29 J. Zhang, X. F. Chen, H. B. Wei and X. H. Wan, *Chem. Soc. Rev.*, 2013, **42**, 9127–9154.
30 J. F. Reuther, D. A. Siriwardane, R. Campos and B. M. Novak, *Macromolecules*, 2015, **48**, 6890–6899.
31 C. A. Dai, W. C. Yen, Y. H. Lee, C. C. Ho and W. F. Su, *J. Am. Chem. Soc.*, 2007, **129**, 11036–11038.
32 C. A. Fustin, N. Lefevre, R. Hoogenboom, U. S. Schubert and J. F. Gohy, *J. Colloid Interface Sci.*, 2009, **332**, 91–95.
33 P. Bhargava, Y. Tu, J. X. Zheng, H. Xiong, R. P. Quirk and S. Z. D. Cheng, *J. Am. Chem. Soc.*, 2007, **129**, 1113–1121.
34 T. J. Giammaria, F. Ferrarese Lupi, G. Seguini, M. Perego, F. Vita, O. Francescangeli, B. Wenning, C. K. Ober, K. Sparnacci, D. Antonioli, V. Gianotti and M. Laus, *ACS Appl. Mater. Interfaces*, 2016, **8**, 9897–9908.
35 D. M. Smilgies, *J. Appl. Crystallogr.*, 2009, **42**, 1030–1034.
36 Y. Yu, L. Zhang and A. Eisenberg, *Macromolecules*, 1998, **31**, 1144–1154.
37 C. Harrison, D. H. Adamson, Z. Cheng, J. M. Sebastian, S. Sethuraman, D. A. Huse, R. A. Register and P. M. Chaikin, *Science*, 2000, **290**, 1558–1560.
38 S. Zhang, C. Cai, Z. Guan, J. Lin and X. Zhu, *Chin. Chem. Lett.*, 2017, **28**, 839–844.
39 L. Onsager, *Ann. N. Y. Acad. Sci.*, 1949, **51**, 627–659.
40 Z. Qiang, L. Zhang, G. E. Stein, K. A. Cavicchi and B. D. Vogt, *Macromolecules*, 2014, **47**, 1109–1116.
41 C. M. Bates, T. Seshimo, M. J. Maher, W. J. Durand, J. D. Cushen, L. M. Dean, G. Blachut, C. J. Ellison and C. G. Willson, *Science*, 2012, **338**, 775–779.
42 M. J. Maher, C. M. Bates, G. Blachut, S. Sirard, J. L. Self, M. C. Carlson, L. M. Dean, J. D. Cushen, W. J. Durand, C. O. Hayes, C. J. Ellison and C. G. Willson, *Chem. Mater.*, 2014, **26**, 1471–1479.
43 K. Yue, C. Liu, M. J. Huang, J. H. Huang, Z. Zhou, K. Wu, H. Liu, Z. W. Lin, A. C. Shi, W. B. Zhang and S. Z. D. Cheng, *Macromolecules*, 2017, **50**, 303–314.
44 L. Y. Shi, S. Lee, L. C. Cheng, H. Huang, F. Liao, R. Ran, K. G. Yager and C. A. Ross, *Macromolecules*, 2019, **52**, 679–689.
45 V. Pryamitsyn and V. Ganesan, *J. Chem. Phys.*, 2004, **120**, 5824–5838.
46 K. Nickmans, J. N. Murphy, B. de Waal, P. Leclère, J. Doise, R. Gronheid, D. J. Broer and A. P. H. J. Schenning, *Adv. Mater.*, 2016, **28**, 10068–10072.
47 K. Nickmans and A. P. H. J. Schenning, *Adv. Mater.*, 2018, **30**, 1703713.
48 C. Cai, J. Lin, Y. Lu, Q. Zhang and L. Wang, *Chem. Soc. Rev.*, 2016, **45**, 5985–6012.
49 W. Zhu, J. Lin, C. Cai and Y. Lu, *J. Mater. Chem. B*, 2013, **1**, 841–849.
50 C. Cai, J. Lin, Z. Zhuang and W. Zhu, *Adv. Polym. Sci.*, 2013, **259**, 159–199.
51 J. Lin, A. Abe, H. Furuya and S. Okamoto, *Macromolecules*, 1996, **29**, 2584–2589.
52 C. Cai, L. Wang, J. Lin and X. Zhang, *Langmuir*, 2012, **28**, 4515–4524.
53 N. Jiang, J. Shang, X. Di, M. K. Endoh and T. Koga, *Macromolecules*, 2014, **47**, 2682–2689.
54 J. M. V. A. Koelman and P. J. Hoogerbrugge, *Europhys. Lett.*, 1993, **21**, 363–368.
55 R. D. Groot and P. B. Warren, *J. Chem. Phys.*, 1997, **107**, 4423–4435.
56 Q. Zhang, J. Lin, L. Wang and Z. Xu, *Prog. Polym. Sci.*, 2017, **75**, 1–30.
57 Z. Guan, L. Wang, X. Zhu and J. Lin, *Mater. Chem. Front.*, 2017, **1**, 697–708.
58 Z. Xu, J. Lin, Q. Zhang, L. Wang and X. Tian, *Polym. Chem.*, 2016, **7**, 3783–3811.